Available online at www.sciencedirect.com
ScienceDirect
Ocean Modelling 18 (2007) 122–141
Ocean Modelling
www.elsevier.com/locate/ocemod

Effects of vertical variations of thickness diffusivity in an ocean general circulation model

Gokhan Danabasoglu [a,*], John Marshall [b]

[a] National Center for Atmospheric Research, P.O. Box 3000, Boulder, CO 80307, USA
[b] Department of Earth, Atmospheric, and Planetary Sciences, Massachusetts Institute of Technology, Cambridge, MA 02139-4307, USA

Received 19 October 2006; received in revised form 26 March 2007; accepted 27 March 2007
Available online 1 May 2007

Abstract

The effects of a prescribed surface intensification of the thickness (and isopycnal) diffusivity on the solutions of an ocean general circulation model are documented. The model is the coarse resolution version of the ocean component of the National Center for Atmospheric Research (NCAR) Community Climate System Model version 3 (CCSM3). Guided by the results of Ferreira et al. (2005) [Ferreira, D., Marshall, J., Heimbach, P., 2005. Estimating eddy stresses by fitting dynamics to observations using a residual-mean ocean circulation model and its adjoint. J. Phys. Oceanogr. 35, 1891–1910.] we employ a vertical dependence of the diffusivity which varies with the stratification, N^2, and is thus large in the upper ocean and small in the abyss. We experiment with vertical variations of diffusivity which are as large as 4000 $m^2 s^{-1}$ within the surface diabatic layer, diminishing to 400 $m^2 s^{-1}$ or so by a depth of 2 km. The new solutions compare more favorably with the available observations than those of the control which uses a constant value of 800 $m^2 s^{-1}$ for both thickness and isopycnal diffusivities. These include an improved representation of the vertical structure and transport of the eddy-induced velocity in the upper-ocean North Pacific, a reduced warm bias in the upper ocean, including the equatorial Pacific, and improved southward heat transport in the low- to mid-latitude Southern Hemisphere. There is also a modest enhancement of abyssal stratification in the Southern Ocean.

Keywords: Ocean general circulation model; Mesoscale eddy parameterization; Vertically varying thickness diffusivity

1. Introduction

Mesoscale eddies contain most of the kinetic energy in the ocean yet cannot be routinely resolved by the global Ocean General Circulation Models (OGCMs) used in long climate simulations. A parameterization that has been widely used to represent their transfer properties in non-eddy-resolving OGCMs is the Gent and McWilliams (1990, hereafter GM90) isopycnal transport parameterization. In GM90, in addition to the diffusion of tracers along isopycnals (Redi, 1982) tracers are advected by the residual circulation, the

* Corresponding author. Tel.: +1 303 497 1604; fax: +1 303 497 1700.
E-mail address: gokhan@ucar.edu (G. Danabasoglu).

1463-5003/$ - see front matter © 2007 Elsevier Ltd. All rights reserved.
doi:10.1016/j.ocemod.2007.03.006

sum of the Eulerian-mean and eddy-induced velocities. The eddy-induced velocity is assumed to be directly proportional to the isopycnal slope with the 'constant of proportionality' interpretable as a diffusivity coefficient – sometimes referred to as the thickness diffusivity. Typically, a constant value of $\mathcal{O}(1000)$ m^2 s^{-1} is used which does not vary in space and time, except near boundaries where 'tapering' recipes are employed for numerical stability. The choice of the constant value of the diffusivity is guided in part by the desire to obtain a model Antarctic Circumpolar Current (ACC) transport that matches observations – larger thickness diffusivity produces enhanced vertical momentum flux, thus supporting more drag with weaker ACC flow (Danabasoglu and McWilliams, 1995).

Estimates of the magnitude of the eddy diffusivity can be deduced from observations (from tracers, floats, drifters, altimetry, moorings, etc. – see e.g., Ledwell et al., 1998; Bauer et al., 1998; Sundermeyer and Price, 1998; Zhurbas and Oh, 2003; Marshall et al., 2006). These observations also tell us that the eddy diffusivity is not constant but exhibits considerable variability in space and time. Prescriptions for the computation of spatial dependencies of the diffusivities have been the subject of many numerical and theoretical studies. Marshall (1981), Treguier et al. (1997), Killworth (1997) and Treguier (1999) for example, focus on prescriptions for the vertical variation of the diffusivity guided by linear baroclinic instability theory and potential vorticity transfer. Danabasoglu and McWilliams (1995) explore the sensitivity of model solutions to an exponential decay of the diffusivities with depth to crudely represent the expected enhancement of mesoscale activity in the upper-ocean. The same exponentially decaying diffusivities are also tested in Jochum (1997). Held and Larichev (1996) and Visbeck et al. (1997) instead, attempt to understand gross horizontal variations of the diffusivity by relating it to the local Eady growth rate or typical eddy length and time scales that depend on some vertically integrated flow properties. A recent proposal by Griffies et al. (2005) takes into account a model's horizontal grid resolution and reduces the thickness diffusivity, particularly in regions of tropical grid refinement, assuming that eddies/tropical instability waves are (partially) resolved there. In addition to observations and theory, the output of eddy-resolving OGCMs have been utilized to estimate both the magnitude and spatial distributions of the thickness diffusivity (e.g., Rix and Willebrand, 1996; Bryan et al., 1999). These studies highlight the importance of the rotational component of eddy fluxes noted by Marshall and Shutts (1981) and Marshall (1984) (more often than not ignored in observational studies) as well as the need for long data sets to obtain robust estimates. Although the rotational component of the eddy flux does not need to be parameterized because it has no effect on the mean equations of motion, it introduces significant complications when diagnosing eddy fluxes in models and data and their association with diffusivities.

Despite the numerous above-mentioned studies, a common approach in the modeling community remains to ignore spatial variations altogether, unless it can be demonstrated that solutions of a particular model are 'improved', e.g., Griffies et al. (2005). This is perhaps because although there is an intellectual recognition that variations should be allowed, it is not at all obvious how one proceeds, there is insufficient observational and theoretical guidance and, often, only marginal improvements in the climatology of the model result when variations are allowed.

An alternative strategy to studying eddy parameterization was recently pursued by Ferreira et al. (2005) who used the adjoint of a large-scale global model – the MITgcm, Marshall et al. (1997a,b) – to fit it to observations by adjusting uncertain parameters. A residual-mean version of the model was used in which the effect of eddies appears in the momentum equations as the vertical divergence of an eddy stress. These eddy stresses were used as control parameters in an optimization procedure which minimized the model drift from observations. The implied eddy diffusivities showed a very substantial variability both in the horizontal and vertical, reaching as high as 4000 m^2 s^{-1} in the upper ocean (see Section 6a of Ferreira et al. (2005) for a more complete discussion, including the presence of (likely spurious) negative diffusivities in the tropics). Below the model thermocline, the model diffusivities are more than an order of magnitude smaller. They suggest that this vertical variation of diffusivity can be usefully captured by assuming that it varies in the same manner as the stratification, N^2. Ferreira et al. (2005) and Ferreira and Marshall (2006) show preliminary, promising results from simulations with the MITgcm using an N^2-dependent formulation for the eddy diffusivities. We note that both the magnitude, range, and surface intensification of the thickness diffusivity reported by Ferreira et al. (2005) have found recent support in Eden et al. (submitted) and Eden (2006) who diagnosed eddy fluxes from high resolution regional OGCMs, carefully taking into account rotational fluxes. In another recent study, Canuto and Dubovikov (2006) propose a diffusivity that varies in the vertical in the same manner as the

mesoscale kinetic energy. This also produces similar vertical variations in diffusivity to those seen in Ferreira et al. (2005).

In this study we perform a detailed assessment of the impacts of a surface-intensified eddy diffusivity formulation proposed by Ferreira et al. (2005) in the ocean component of the National Center for Atmospheric Research (NCAR) Community Climate System Model version 3 (CCSM3), comparing its solutions to those obtained using a spatially uniform thickness diffusivity. Our mesoscale eddy parameterization combines the GM90 parameterization in the interior with the near-boundary eddy flux parameterization of Ferrari and McWilliams (submitted) in the surface diabatic layer, as detailed in Danabasoglu et al. (submitted). We regard use of an N^2 dependency as a convenient way of introducing a surface intensification of the diffusivity coefficient. Finally we note that in the planetary quasi-geostrophic limit the GM90 parameterization that uses an N^2-dependent vertical thickness diffusivity (as in the present study) is equivalent to an eddy stress parameterization (for the momentum equations) that is cast in terms of the vertical shear of the currents which employs a constant vertical eddy viscosity (as in Ferreira and Marshall, 2006) – see, for example, Greatbatch and Lamb (1990) and Gent et al. (1995).

The structure of our paper is as follows. In Section 2, we briefly describe the OGCM and our implementation of the N^2-dependent eddy diffusivity. The results are presented in Section 3. Finally, Section 4 contains a summary and our concluding remarks.

2. Ocean model

The ocean model is based on the Parallel Ocean Program (POP 1.4) of the Los Alamos National Laboratory (Smith and Gent, 2004) and is used as the ocean component of the NCAR CCSM3. It is a global, level-coordinate model with the grid North Pole displaced into Greenland. In this study, we use the nominal 3° horizontal resolution version of the model (Yeager et al., 2006). The resolution is uniform at 3.6° in the zonal direction, but varies in the meridional direction. The finest meridional grid spacing occurs at the high latitudes of the northeast Atlantic and at the equator with 0.4° and 0.6°, respectively. The Southern Hemisphere mid-latitudes and far northwest Pacific have the coarsest meridional resolution of about 3°. There are 25 vertical levels, monotonically increasing from 8 m near the surface to about 500 m in the abyssal ocean.

The surface fluxes of heat, salt, and momentum are computed using the bulk forcing scheme detailed in Large et al. (1997) and Large and Yeager (2004). The *normal year* data sets developed by Large and Yeager (2004) are utilized in all the present simulations. The net surface heat flux shows a negative bias of about 5 W m^{-2}, when these data sets are used with the observed sea surface temperatures (a blending of Levitus et al. (1998) and Steele et al. (2001) data sets). Therefore, this bias is crudely eliminated by uniformly adding 5 W m^{-2} to the downward long-wave heat flux component. A global factor computed based on the change in the global-mean salinity during a year is used to multiply both precipitation and runoff fluxes to partially balance the evaporation for the next year. This factor remains close to unity, equilibrating at 1.01. In addition, a weak salinity restoring is applied globally, using monthly-mean climatological salinities (again a blending of Levitus et al. (1998) and Steele et al. (2001) data sets). This restoring coefficient is 11.5 mg m^{-2} s^{-1} psu^{-1}, corresponding to a 232-day time scale over 8 m (the model's first vertical level thickness). The global mean of this restoring flux is subtracted every model time step, so it does not contribute to the global salt budget. We do not use an active sea–ice model. However, under ice covered regions, we apply monthly-mean freshwater fluxes diagnosed from a coupled ocean–ice integration. Further details of these data sets and forcing formulation, including treatment for river runoff, are given in Large and Yeager (2004) and Danabasoglu (2004).

The momentum equations use the anisotropic horizontal viscosity formulation of Large et al. (2001), as generalized by Smith and McWilliams (2003). These viscosity coefficients differ arbitrarily along the grid directions and the minimum horizontal viscosity is set to 1000 m^2 s^{-1} unless numerical stability requires lower values. The vertical mixing coefficients are determined using the K-Profile Parameterization (KPP) of Large et al. (1994), as modified by Danabasoglu et al. (2006). In the ocean interior, similar to Bryan and Lewis (1979) the background internal wave mixing diffusivity varies in the vertical from 0.1×10^{-4} m^2 s^{-1} near the surface to 1.0×10^{-4} m^2 s^{-1} in the abyssal ocean. The transition to larger values occurs at a depth of about 1000 m to crudely represent enhanced mixing over rough topography (Ledwell et al., 2000). Due to double diffusion, the vertical mixing coefficients for potential temperature and salinity may differ. The vertical

viscosity has the same shape as the vertical diffusivity, but 10 times larger, i.e., the turbulent Prandtl number is 10. Both the vertical viscosity and diffusivity coefficients are increased to $1000 \times 10^{-4}\ \mathrm{m^2\ s^{-1}}$ whenever static instability is detected in the ocean interior.

A preliminary version of the near-surface eddy flux parameterization of Ferrari and McWilliams (submitted) as implemented by Danabasoglu et al. (submitted) is used in the tracer equations in all the numerical experiments. In this parameterization, a transition layer separates the quasi-adiabatic interior where eddy fluxes are oriented along isopycnals from the diabatic, near-surface regions (e.g., the boundary layer) where diapycnal mesoscale fluxes are directed along the ocean surface. In the interior, eddy fluxes are represented using the isopycnal diffusion tensor (Redi, 1982; Cox, 1987) and the GM90 isopycnal transport parameterization with its eddy-induced velocity. We use A_{I} and A_{ITD} to denote the respective isopycnal and thickness diffusivities. As the surface is approached, the mesoscale eddy fluxes become parallel to the ocean surface, crossing outcropping density surfaces. This behavior is parameterized using a down-gradient horizontal diffusion with a mixing coefficient of A_{H}, and represents the only eddy mixing within the boundary layer. A_{H} has the same value as the interior A_{I}, indicating that the interior and near-surface mixing rates remain the same. A linear combination of horizontal and isopycnally-oriented mixing occurs within the transition layer. The eddy-induced velocity is parallel to the ocean surface and has no vertical shear within the boundary layer. It must then develop vertical shear within the transition layer to match the interior values. In Danabasoglu et al. (submitted) the surface diabatic layer depth (DLD) is formally defined as the sum of the boundary layer depth and the transition layer thickness. However, they obtain similar DLD distributions when the boundary layer depth is replaced with the mixed layer depth (as defined in Large et al., 1997). Danabasoglu et al. (submitted) further show that the model solutions are not very sensitive to the transition layer thickness, and hence presumably to the details of the formulation there. Further details of the mesoscale eddy parameterization are given in Danabasoglu et al. (submitted).

As suggested by Ferreira et al. (2005) and Ferreira and Marshall (2006) the vertical variation of A_{ITD} is specified using

$$A_{\mathrm{ITD}} = \left[\frac{N^2}{N^2_{\mathrm{ref}}}\right] [A_{\mathrm{ITD}}]_{\mathrm{ref}}, \tag{1}$$

where N is the local buoyancy frequency computed at the vertical level interfaces and $\left[A_{\mathrm{ITD}}\right]_{\mathrm{ref}}$ is the constant reference value of A_{ITD} within the surface diabatic layer. N_{ref} is the reference buoyancy frequency obtained just below DLD, provided that $N^2 > 0$ there. Otherwise N^2_{ref} is the first stable N^2 below DLD. In both situations, the ratio N^2/N^2_{ref} is set to 1 for all shallower depths, implying no vertical variation of A_{ITD}, particularly within the surface diabatic layer. Between the depth at which $N^2 = N^2_{\mathrm{ref}}$ and the ocean bottom, we also ensure that

$$N_{\mathrm{min}} \leqslant \frac{N^2}{N^2_{\mathrm{ref}}} \leqslant 1.0, \tag{2}$$

where N_{min} (>0) is a specified lower limit. Eq. (2) also implies that in statically unstable regions, i.e. $N^2 < 0$, $N^2/N^2_{\mathrm{ref}} = 0.1$. This approach ensures the vertical smoothness of the N^2/N^2_{ref} profile and relies on the enhancement of vertical mixing coefficients to alleviate any local static instability.

In our present experiments with vertically varying A_{ITD}, the N^2/N^2_{ref} profiles are evaluated at every model time step. However, such frequent computation of these profiles is probably unnecessary because sensitivity experiments using once-a-day (at the beginning of a day) N^2/N^2_{ref} profile computations produce nearly identical results. We avoid any vertical averaging of the profiles to preserve their extrema. Instead, N^2/N^2_{ref} computed at the top face of a grid cell is simply used for that grid cell. The resulting A_{ITD} from (1) is subject to the usual diffusive numerical stability criterion (Cox, 1987). Here, we use an allowable maximum slope of 0.3, a value much larger than the commonly used value of 0.01 (see Danabasoglu et al. (submitted) for further discussions). In addition, the zero eddy flux boundary condition at the ocean bottom is imposed by setting the diffusivities to zero in the bottom halves of the grid boxes. Thus, the effective A_{ITD} for these bottom grid cells is further reduced by one half.

The numerical experiments are listed in Table 1. CONTROL uses a constant value of $800\ \mathrm{m^2\ s^{-1}}$ for A_{I}, A_{ITD}, and A_{H}, and is identical to case DM of Danabasoglu et al. (submitted). In TN2, A_{ITD} is given by (1)

Table 1
List of numerical experiments

Case	A_{ITD} or $[A_{ITD}]_{ref}$ ($m^2\ s^{-1}$)	A_I ($m^2\ s^{-1}$)	A_H ($m^2\ s^{-1}$)	N_{min}	ACC (Sv)	$\langle\theta\rangle$ (°C)	$\langle$SHF$\rangle$ (W m^{-2})
CONTROL	800	800	800		130	3.74	−0.019
TN2	4000 (1)	800	800	0.1	155	3.51	−0.039
TN2_LOW	4000 (1)	800	800	0.01	196	3.83	
ITN2	4000 (1)	4000 (1)	4000	0.1	124	3.46	−0.034

ACC is the Antarctic Circumpolar Current transport at Drake Passage, $\langle\theta\rangle$ is the global-mean potential temperature, and $\langle$SHF$\rangle$ is the global-mean surface heat flux. ACC, $\langle\theta\rangle$ and $\langle$SHF$\rangle$ are the year 2000 mean values, except for TN2_LOW. (1) refers to Eq. (1) given in Section 2.

with $[A_{ITD}]_{ref} = 4000\ m^2\ s^{-1}$ and $N_{min} = 0.1$. Here, $A_I = A_H = 800\ m^2\ s^{-1}$. TN2_LOW is the same as TN2 except that $N_{min} = 0.01$, thus allowing much smaller thickness diffusivities in the abyssal ocean. Our final case, ITN2, uses (1) to evaluate both A_I and A_{ITD} and sets $A_I = A_{ITD}$ with $[A_I]_{ref} = [A_{ITD}]_{ref} = A_H = 4000\ m^2\ s^{-1}$ and $N_{min} = 0.1$. Such use of equal diffusivities is a common practice in many OGCM applications, mostly for simplicity. We note that, at least for the case of constant diffusivities, the theoretical study of Dukowicz and Smith (1997) supports specifying equal values. All of the experiments are initialized with the January-mean potential temperature and salinity climatology (Levitus et al., 1998; Steele et al., 2001 for the Arctic Ocean) and zero velocity. CONTROL, TN2, and ITN2, integrated for 2000 years each, are our primary cases. TN2_LOW is integrated for only 500 years. Unless otherwise noted, our analysis is based on the time-mean data for the last 20 years of integration.

3. Results

After 2000 years of integration, trends in the model global-mean potential temperatures remain as indicated by the non-zero global-mean surface heat flux values of Table 1. However, these drifts are very small, e.g., we estimate a maximum expected drift of 0.008 °C in global-mean potential temperature during an additional 100-year integration of TN2. As a result of our forcing procedure, there are no drifts in the global-mean salinity value. Table 1 also records the ACC transport at Drake Passage for all cases. The observational estimate of this transport is 134 ± 13 Sv (Whitworth, 1983; Whitworth and Peterson, 1985). Thus both CONTROL and ITN2 transports lie within the observational range, while the transport is larger than the estimates by 8 Sv in TN2. Clearly, 196 Sv in TN2_LOW (discussed in the Appendix) is excessively large.

The distributions of the reference buoyancy frequency squared, surface diabatic layer depth, the upper-ocean and zonal-mean thickness diffusivity; along with the zonal-mean normalized buoyancy frequency squared from TN2 are given in Fig. 1. The spatially averaged plots exclude the near-surface diabatic layer because A_{ITD} values there are not used in the eddy-induced velocity computations (see Danabasoglu et al., submitted). The N^2_{ref} spatial patterns (Fig. 1a) largely reflect those of the diabatic layer depth (Fig. 1b), i.e., the regions of high (low) N^2_{ref} coincide with the regions of shallow (deep) diabatic layer depth. N^2_{ref} is particularly large in the eastern parts of the basins at low latitudes and in the Arctic Ocean. The Kuroshio and Gulf Stream paths also show modest values. Elsewhere, N^2_{ref} is less than $3 \times 10^{-4}\ s^{-2}$ with the Southern Ocean latitude band having the smallest value ($<1 \times 10^{-4}\ s^{-2}$). By construction, i.e., see (1), the A_{ITD} distributions follow that of N^2/N^2_{ref} as evidenced by the similarity of the zonal-mean patterns of A_{ITD} and N^2/N^2_{ref} shown in Figs. 1e and f. The upper-ocean distributions (Figs. 1c and d) reveal that the largest values of A_{ITD} ($>1250\ m^2\ s^{-1}$) occur in areas of low N^2_{ref} and broadly coincide with the regions of expected intense eddy activity, i.e., the ACC and western boundary currents. As the model fields evolve from their initial conditions, there are modest changes in the strength and distribution of A_{ITD} (Fig. 1d). An example is the southward shift of the large A_{ITD} region in the mid-latitude North Atlantic as a result of the changes in the path of the model Gulf Stream. Another change occurs in the ACC as evidenced by broadening of the area where $A_{ITD} > 1500\ m^2\ s^{-1}$. In general, larger A_{ITD} values tend to occur on the equatorward side of ACC, particularly evident in Fig. 1c. In their inferred surface diffusivity distributions, Ferreira et al. (2005) also note the same feature which is attributed to the presence of strong potential vorticity gradients along the axis of ACC, thus limiting lateral dispersal of water parcels (Marshall et al., 2006). Perhaps the least desirable feature of the A_{ITD} distributions is

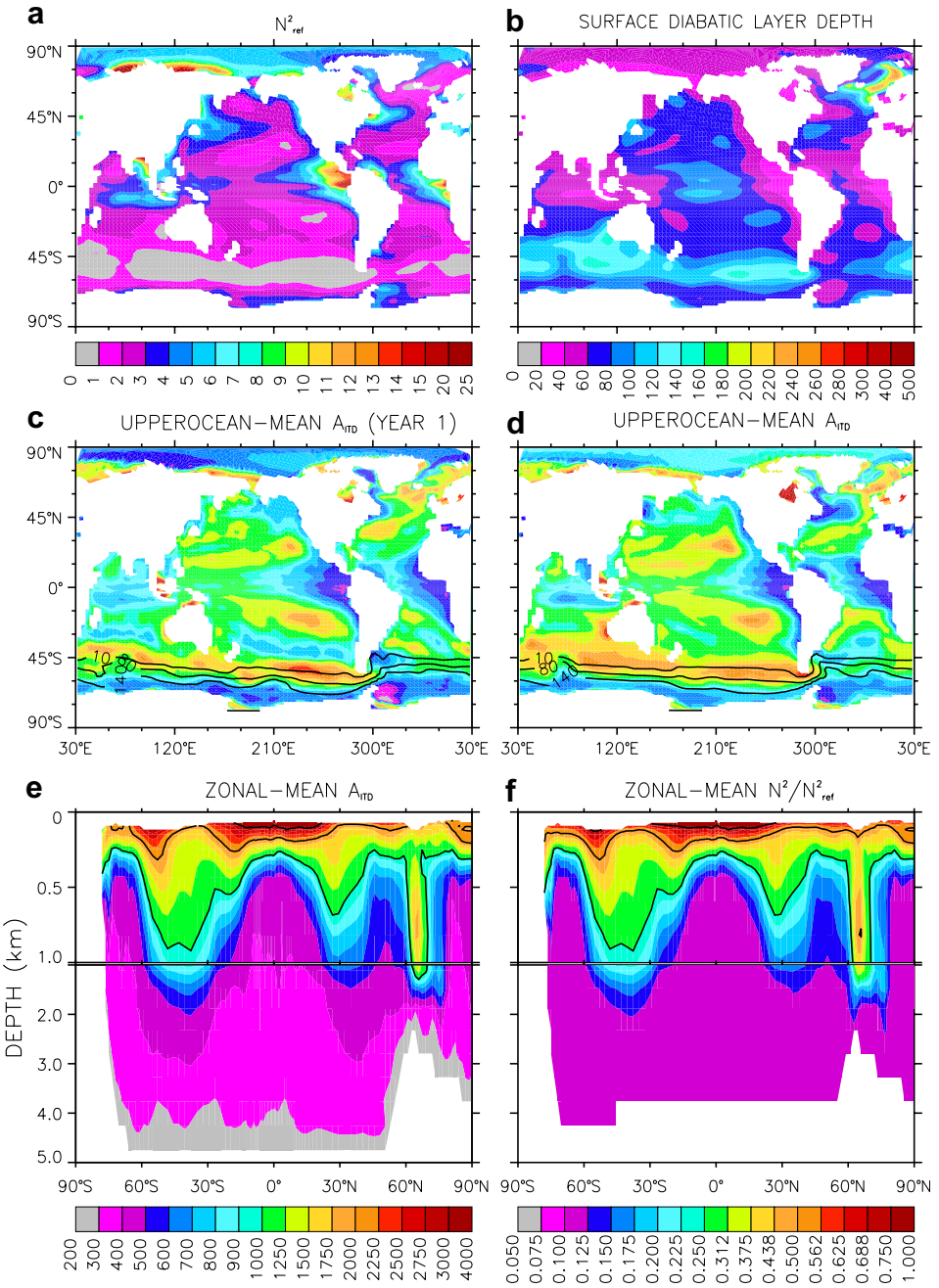

Fig. 1. (a) Reference buoyancy frequency squared, N^2_{ref}, in 10^{-4} s^{-2}; (b) Surface diabatic layer depth in m; Upper-ocean [0–945 m]-mean thickness diffusivity coefficient, A_{ITD}: (c) year 1 mean and (d) years (1981–2000) mean; Zonal-mean, global (e) A_{ITD} and (f) N^2/N^2_{ref}. All panels except (c) show years (1981–2000) mean. All panels are from TN2. Panels (c–e) are in m^2 s^{-1} and share the same contour intervals. In (f), the contour intervals are obtained by normalizing the contour intervals used in panels (c–e) by $[A_{ITD}]_{ref}$ (see Eq. (1)). In (c) and (d), 10, 80, and 140 Sv contour lines are drawn for the Antarctic Circumpolar Current transport. In (e), 1000, 2000, and 3000 m^2 s^{-1} contour lines are indicated. The corresponding N^2/N^2_{ref} contours of 0.25, 0.50, and 0.75 are also drawn in (f).

the region where $A_{ITD} > 1750$ m^2 s^{-1} in the eastern South Pacific. The zonal-mean distribution (Fig. 1e) shows that the largest diffusivities (>3000 m^2 s^{-1}) are found in the tropical oceans, just below the diabatic layer. However, these large diffusivities are confined to the upper ocean, rapidly decaying to values of 400 m^2 s^{-1}

by a depth of 400 m or so. Similar vertical structures are also observed at high latitudes, but with smaller upper-ocean diffusivities. In contrast, the deepest penetration of large A_{ITD} occurs at mid-latitudes. Nevertheless, by about 2000-m depth, the minimum specified value of 400 $\mathrm{m^2\,s^{-1}}$ (save for tapering and near-boundary treatment) is attained at all latitudes.

Roemmich and Gilson (2001) provide an observational estimate of the eddy-induced transports in the upper ocean along a repeated hydrographic line in the North Pacific at an average latitude of 22°N. We present a comparison of our model eddy-induced transports obtained along the same transect with their observational estimate in Fig. 2. Transports are given in temperature classes with a bin interval of 1 °C and the cumulative northward and southward transports are listed in each panel. The vertical variations in eddy-induced transport in ITN2 and TN2, as well as the cumulative transports, are in remarkably good agreement with these observational estimates. In contrast, the transports in CONTROL are lower than observed by a factor of 2.4–4.8. In ITN2 and TN2, the vertical variations in thickness diffusivity are largely responsible for these beneficial eddy-induced velocity distributions. The eddy-induced meridional current, v^*, is given by

$$v^* = -\frac{\partial(A_{\mathrm{ITD}} S_y)}{\partial z} = -\left(\frac{\partial A_{\mathrm{ITD}}}{\partial z} S_y + A_{\mathrm{ITD}} \frac{\partial S_y}{\partial z}\right), \tag{3a}$$

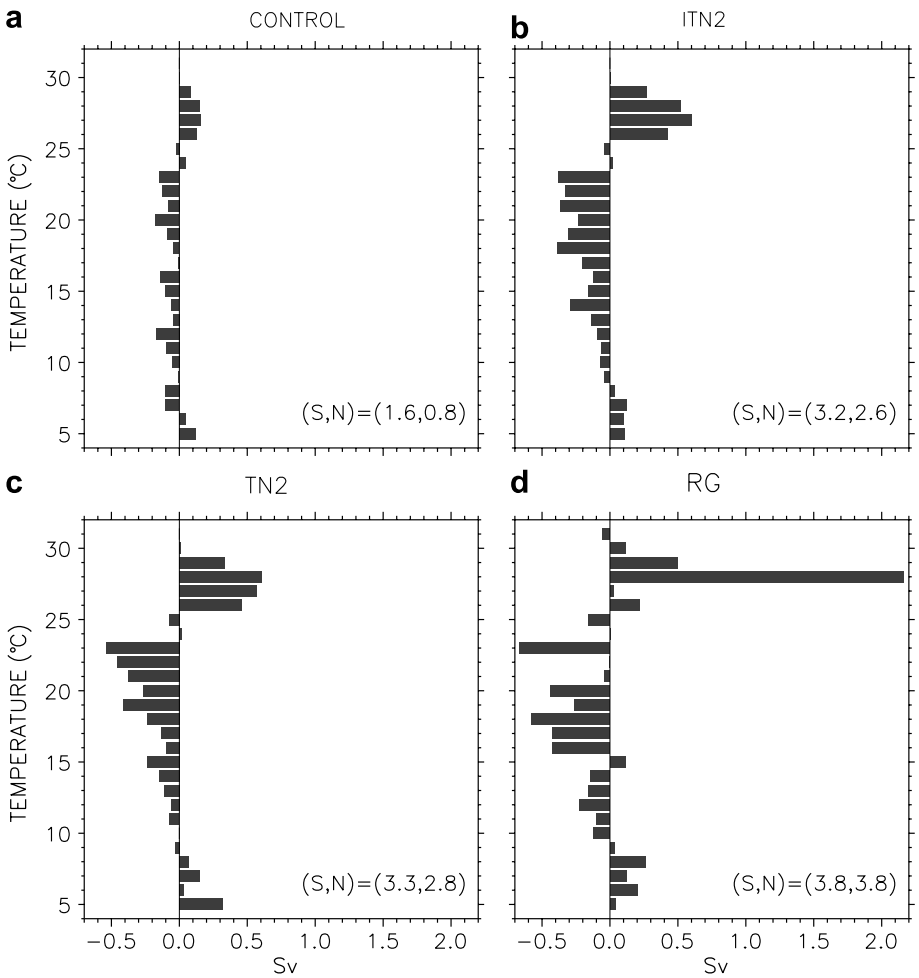

Fig. 2. Time-mean, eddy-induced normal transport in potential temperature bins (1 °C bin interval) in the upper-ocean integrated along the repeated hydrographic ship track in the tropical North Pacific from (a) CONTROL, (b) ITN2, (c) TN2, and (d) measured by Roemmich and Gilson (2001). The numbers denoted by S and N indicate the cumulative southward and northward transports in the upper ocean, respectively. The integrals extend to 945 and 800 m in the model and observations, respectively.

with

$$\int v^* \, \mathrm{d}x = -\frac{\partial \Psi^*}{\partial z}, \tag{3b}$$

where Ψ^* is the streamfunction for the eddy-induced transport, S_y is the meridional slope of the isopycnal surfaces, z is the vertical coordinate, positive upwards, and x denotes the longitudinal direction. Of course in models in which A_{ITD} is kept constant, only the second term in the right hand side (RHS) of (3a) makes a contribution. However, as can be seen in Fig. 3, because the diffusivities now markedly increase as the surface is approached, the first term in the RHS of (3a) makes the major contribution and, in fact, is largely responsible for improvements in the thermocline of the model. Note that McWilliams and Danabasoglu (2002) argue that an increase in the magnitude of A_{ITD} can improve model performance. Here the vertical variation of A_{ITD} is the key factor.

We examine the changes in the isopycnal slopes by considering the zonal-mean of its meridional component, i.e., S_y, presented in Fig. 4. In all cases, both the patterns and magnitudes of S_y are generally similar. As expected, the largest slopes occur in the southern and northern high latitudes as well as in the upper ocean. We note that, even in the zonal-mean, $|S_y|$ can be larger than the commonly adopted maximum slope value of 0.01, thus supporting the use of a larger maximum slope value as in the present study. Figs. 4c and e show that the differences of ITN2 and TN2 from CONTROL are similar, again both in magnitude and pattern, with the largest differences mostly co-located with the largest slope regions, e.g., the Southern Ocean and around 60°N latitude. However, even small differences in the vertical gradient of S_y can lead to significant transport differences as indicated by (3). For example, a modest increase of 0.0001 in $|\Delta S_y|$ in the vertical in TN2 compared to ITN2 at about 2500-m depth produces $\mathcal{O}(1\ \mathrm{Sv})$ increase in the eddy-induced overturning circulation in TN2 at 60°S, with $A_{\mathrm{ITD}} = 400\ \mathrm{m^2\ s^{-1}}$ (see Fig. 5).

The zonally-integrated eddy-induced and residual, i.e. Eulerian-mean + eddy-induced, meridional overturning circulations (MOC) from CONTROL, ITN2, and TN2 are presented in Fig. 5. In all three cases, the eddy-induced MOCs (Figs. 5a–c) are dominated by a counter-clockwise circulation that penetrates to the ocean bottom in the Southern Ocean and a much weaker and shallower clockwise circulation in the Northern Hemisphere mid-latitudes. These overturning distributions exhibit similar spatial patterns as those of the zonal-mean meridional isopycnal slopes shown in Fig. 4. This similarity is already expected for uniform A_{ITD} as in CONTROL. As discussed above, vertical variations in A_{ITD} lead to stronger circulations in the upper ocean in ITN2 and TN2 compared to CONTROL, as evidenced by the 12.5 Sv transport (at 300-m depth) of counter-clockwise Southern Ocean circulation in the former cases compared to the 9 Sv transport in CONTROL. Another example is the more vigorous (4–6 Sv) counter-rotating, shallow cells within a few degrees of the equator which are only about 1–2 Sv in CONTROL. In contrast, the maximum Southern Hemisphere

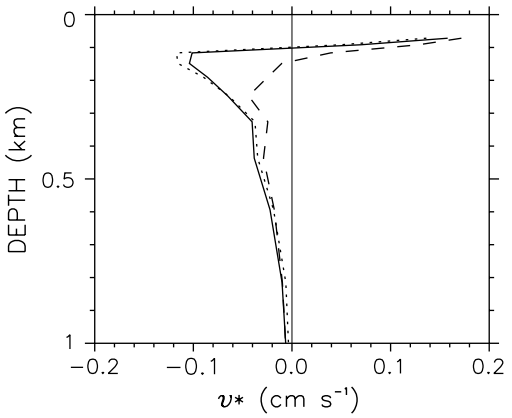

Fig. 3. Upper-ocean profiles of the time- and horizontal-mean meridional component of the eddy-induced velocity (v^*, see (3a)) computed between 20°N and 40°N in the North Pacific. The dashed and solid lines are from CONTROL and ITN2, respectively. The dotted line represents the contribution from $-\frac{\partial A_{\mathrm{ITD}}}{\partial z} S_y$ of (3a) to v^* in ITN2.

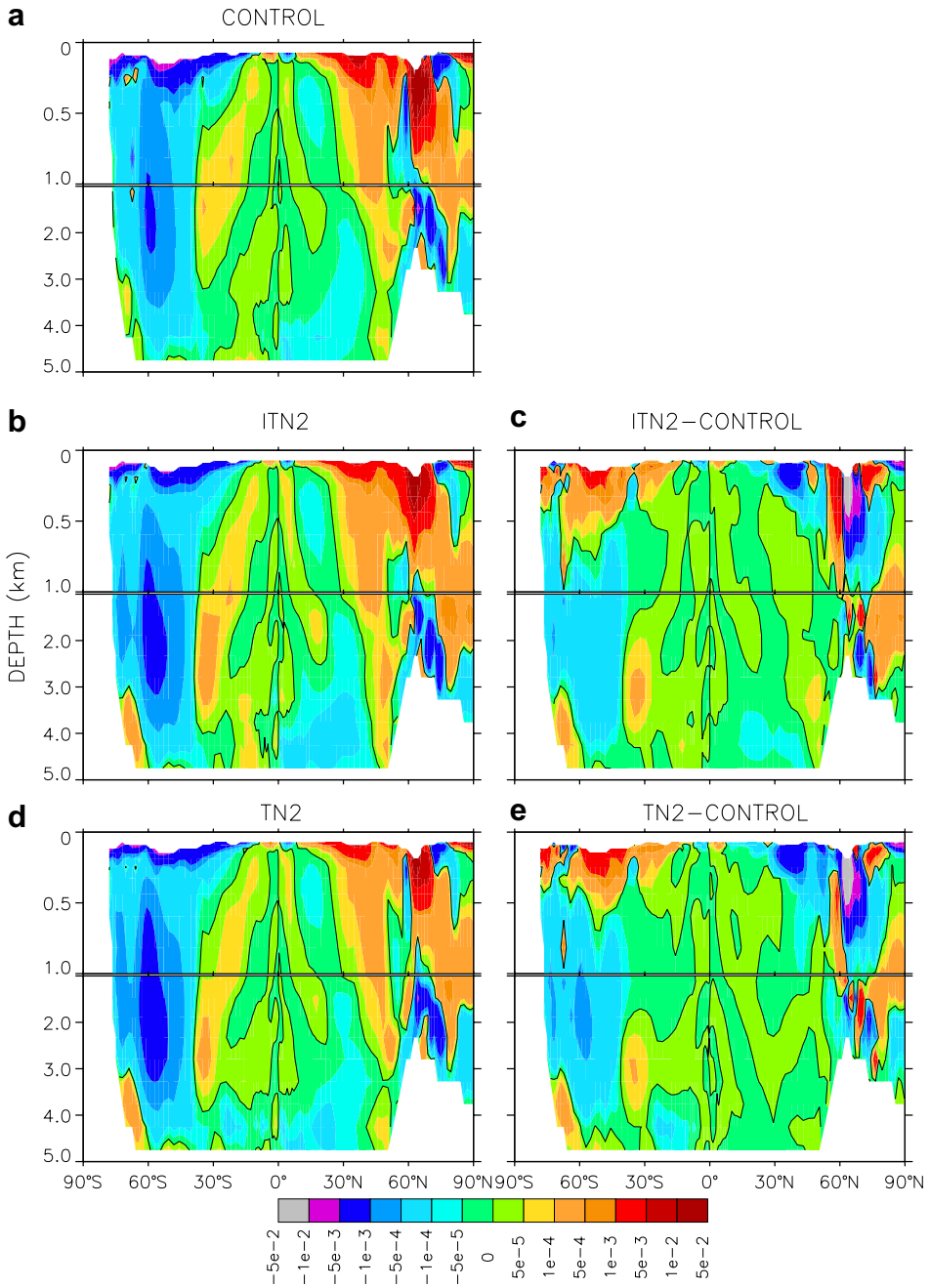

Fig. 4. Time- and zonal-mean meridional component of the isopycnal slope, S_y, (a) from CONTROL, (b) from ITN2, (c) ITN2 – CONTROL difference, (d) from TN2, and (e) TN2 – CONTROL difference. The distributions are global. All panels have the same color scale, and the zero contour lines are marked.

circulations are 19.4, 17.6, and 14.7 Sv in CONTROL, TN2, and ITN2, respectively, indicating a weakening circulation at depth as diffusivities are reduced. A comparison of the eddy-induced circulations computed in density space with a reference depth of 2000 m (not shown) also reveals similarly weaker circulation in higher density classes with reduced diffusivities (18.5, 15.5, and 14.2 Sv in CONTROL, TN2, and ITN2, respectively). These results, i.e., upper-ocean strengthening and abyssal weakening of the eddy-induced circulation with

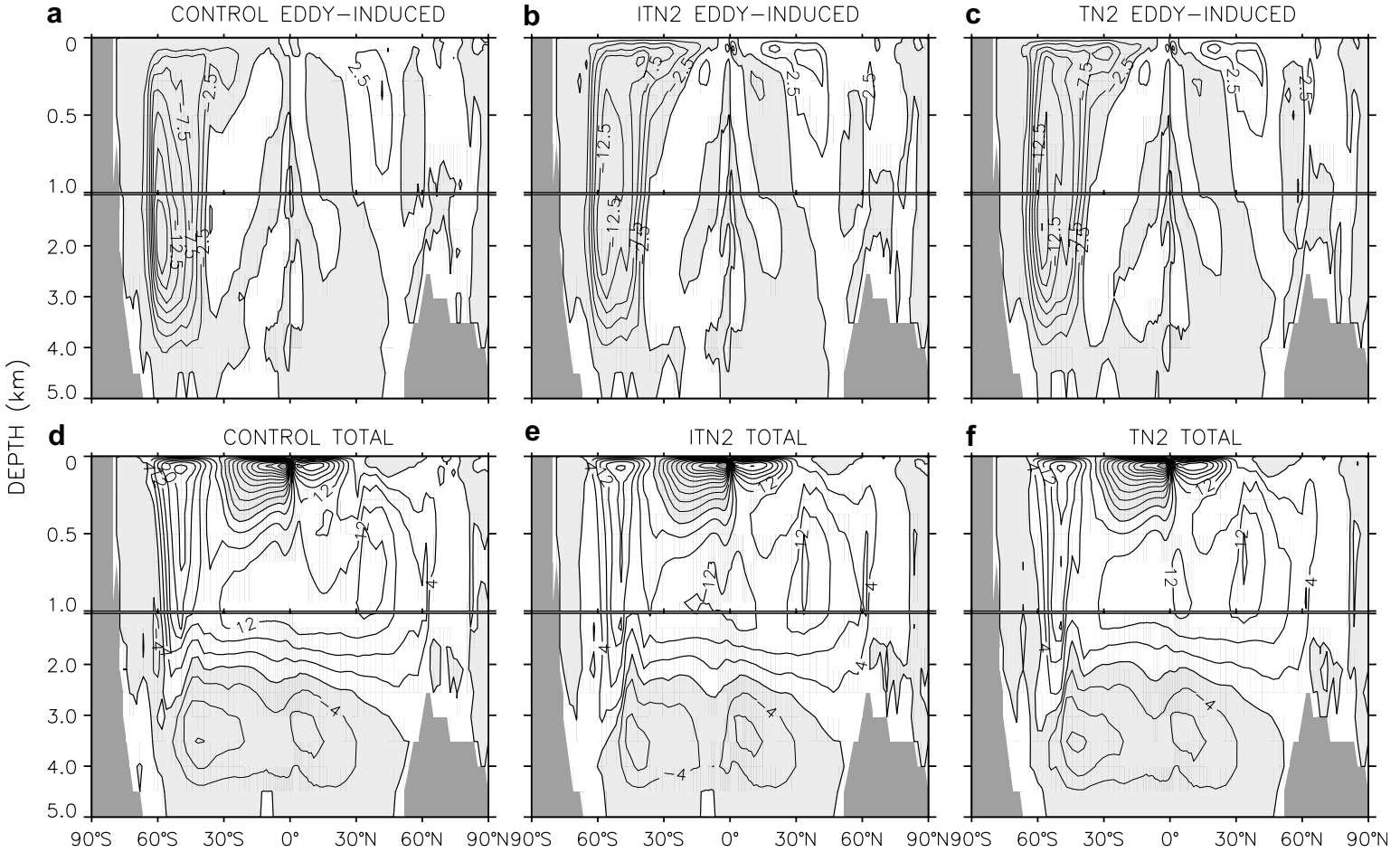

Fig. 5. Time-mean zonally-integrated global meridional overturning streamfunction: Eddy-induced from (a) CONTROL, (b) ITN2, (c) TN2, and residual (i.e., Eulerian-mean + eddy-induced) from (d) CONTROL, (e) ITN2, and (f) TN2. The contour intervals are 2.5 and 4 Sv for panels (a–c) and (d–f), respectively. The thin lines and shading indicate counter-clockwise circulation.

N^2-dependent diffusivities, are consistent with the results of Ferreira and Marshall (2006). In ITN2 and TN2, the increased eddy-induced circulation in the upper ocean at the latitude band of the Southern Ocean cancels more of the Eulerian-mean Deacon cell in the upper 750 m compared to CONTROL (Figs. 5d–f). The circulation associated with the North Atlantic Deep Water (NADW) is weaker by about 2 Sv in ITN2 and TN2 than in CONTROL. However, the downwelling rates across 1000-m depth and between 60°N and 65°N, a measure advocated by Gent (2001), are identical in CONTROL and ITN2 (6.2 Sv), and only slightly lower in TN2 (5.2 Sv). The circulation associated with the Antarctic Bottom Water (AABW) is weaker in ITN2 than in CONTROL and TN2. This AABW weakening in ITN2 is still present when the circulations are computed in density space (not shown). An examination of the ITN2 − CONTROL difference distributions for surface density (not shown) reveals that the surface waters in ITN2 are generally lighter than in CONTROL south of 60°S, including the AABW formation regions (as found in Danabasoglu et al., submitted). These lighter densities penetrate to a depth of about 250 m in the zonal mean and are largely dictated by the surface salinity changes because its contraction coefficient is much larger than the thermal expansion coefficient at these latitudes. Although we do not have a detailed mechanistic explanation for the weakening of AABW, we believe that the reduced upper-ocean density in ITN2 may provide a possible means for the weaker AABW circulation in ITN2. We also speculate that as a result of this weakening, NADW penetrates slightly deeper in ITN2.

As suggested in Figs. 5a–c, the strength of the eddy-induced circulation appears to be also affected by A_I which can have both direct and indirect influences on the distributions of isopycnal slopes. As shown earlier, seemingly small changes in the vertical gradients of isopycnal slopes can result in modest transport changes. The indirect effect, likely the dominant one, is due to changes in the diapycnal processes, resulting from changes in potential temperature and salinity distributions associated with adiabatic diffusive processes controlled by A_I. Although water parcels remain on the same density surfaces when in adiabatic motion, the potential temperature and salinity distributions in the vertical are affected. Surface heat and salt fluxes and vertical diffusivities, including a representation of double-diffusive mixing, act on potential temperature and salinity profiles to further modify vertical distributions. The direct effect can occur due to cabbeling and thermobaricity when using the nonlinear equation of state as in the present model. These two processes can produce diapycnal mixing, thus modifying the isopycnal slopes directly.

Fig. 6 shows the modeled time-mean global northward heat transport, including its component contributions. For comparison purposes, Fig. 6a also includes an estimate of meridional heat transport based on the NCEP data (computed as a residual) from Trenberth and Caron (2000). In the North Atlantic (not shown), the maximum heat transport is 0.76 PW in ITN2 and TN2, lower than the CONTROL transport of 0.85 PW. However, there is a compensating increase in the North Pacific northward heat transport (not shown) in ITN2 and TN2, and therefore the total Northern Hemisphere transports given in Fig. 6a do not differ significantly between cases. We note that both the global and Atlantic Northern Hemisphere heat transports are lower than the available observational estimates (e.g. in the North Atlantic 1.2–1.3 ± 0.3 PW from Bryden and Imawaki, 2001). This is a typical problem of coarse resolution ocean model and can be partially attributed to both the *normal year* data sets used to force the model and a third-order upwind tracer advection scheme. In the Southern Hemisphere, ITN2 and TN2 indicate larger southward heat transport compared to CONTROL, particularly between 5°S and 30°S. This results in a more favorable comparison with the Trenberth and Caron (2000) estimates (Fig. 6a). Further south, ITN2 southward transport remains larger than in CONTROL and TN2, and is only marginally below the estimated uncertainty. The Eulerian-mean and eddy-induced heat transport components (Figs. 6b and c, respectively) have similar distributions in ITN2 and TN2. The transport differences relative to CONTROL in these cases tend to cancel each other. For example, the reduction in the Eulerian-mean northward transport between 15°N and 40°N is partially canceled by the increase in the eddy-induced northward transport. The strengthening of the counter-rotating cells about the equator results in increased southward (northward) eddy-induced heat transport in the Northern (Southern) Hemisphere (Fig. 6c). Consistent with the stronger near-surface eddy-induced circulations in ITN2 and TN2 (Figs. 5a–c), the largest eddy-induced heat transport differences between these cases and CONTROL occur primarily in the Southern Hemisphere. The diffusive component (due to diapycnal horizontal mixing within the surface diabatic layer and isopycnal stirring within the interior) of the meridional heat transport is very similar in CONTROL and TN2 because they employ the same A_I and A_H values (Fig. 6d). In contrast, larger diffusivities, particularly A_H, in the upper ocean lead to higher poleward heat transports in both hemispheres by as

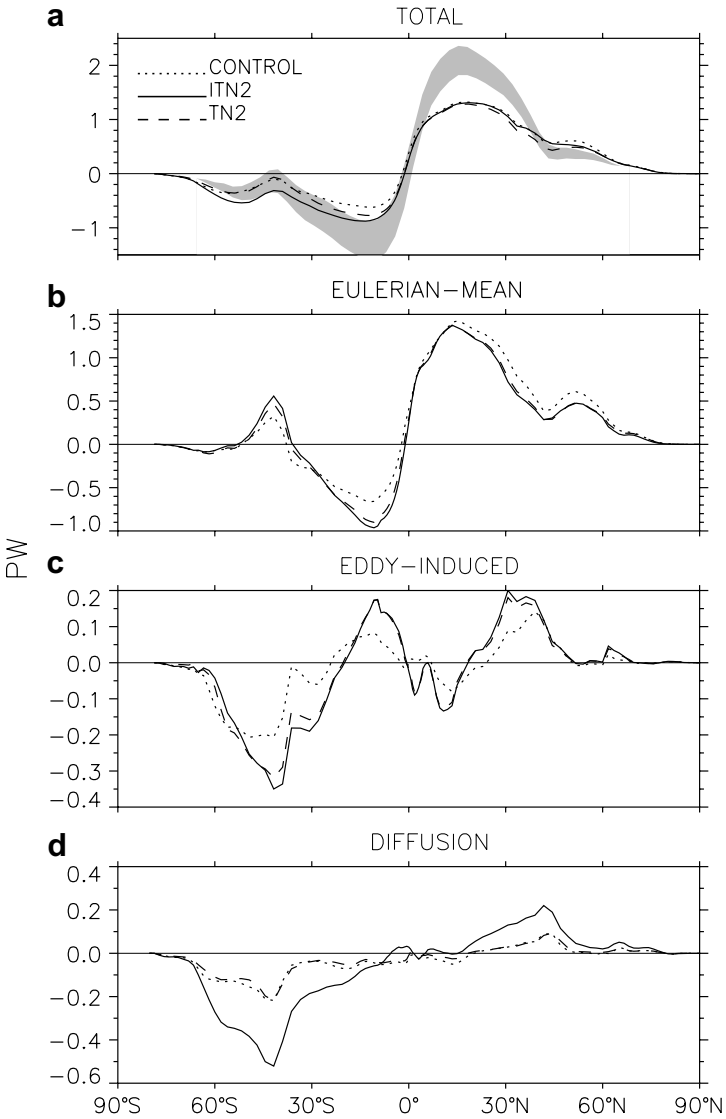

Fig. 6. Time-mean global northward heat transport from CONTROL, ITN2, and TN2: (a) total; (b) Eulerian-mean component; (c) eddy-induced component; (d) diffusion component. The latter includes both isopycnal and horizontal diffusion contributions. In (a), shading indicates one standard error envelope of the residual estimate from Trenberth and Caron (2000) based on NCEP data.

much as 0.3 PW. This increased diffusive contribution is mostly responsible for the larger total transport in ITN2 compared to TN2 throughout the southern latitudes shown in Fig. 6a.

We next consider the ideal age tracer (Thiele and Sarmiento, 1990) to determine changes in ocean ventilation timescales. This tracer uses the same equations as potential temperature and salinity, but with a source term of one unit per year of model integration. All cases are initialized with zero age, and the ideal age tracer is set to zero at the surface at each model time step. Thus, the regions of low ventilation have the oldest waters while the younger waters indicate recent contact with the ocean surface. Fig. 7 shows the time- and zonal-mean global ideal age distributions from ITN2 and TN2 in comparison with CONTROL. The oldest waters have zonal-mean ages of >1500 yr (Figs. 7a and c), occurring in the abyssal Pacific Ocean (not shown). Both ITN2 and TN2 difference distributions (Figs. 7b and d) show that their waters are older than in CONTROL, revealing a general reduction in ventilation. However, there are some regional differences between ITN2 and TN2. First, in contrast to TN2, the ventilation actually increases in the Atlantic Ocean between about

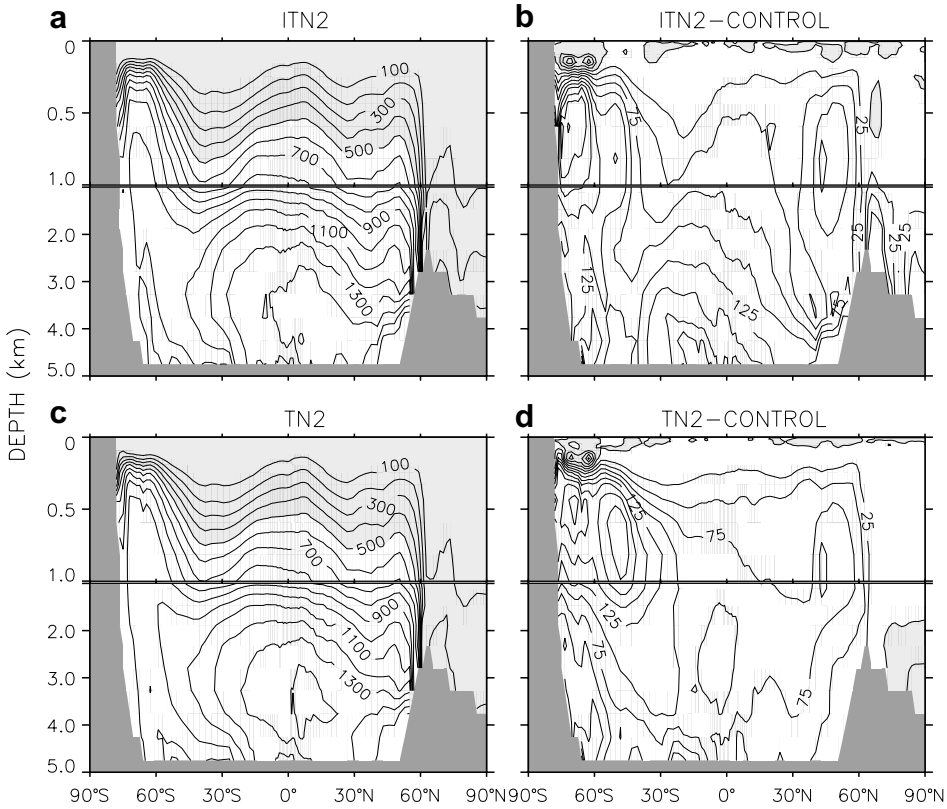

Fig. 7. Time- and zonal-mean, global ideal age (a) from ITN2, (b) ITN2 − CONTROL difference, (c) from TN2, and (d) TN2 − CONTROL difference. In (a) and (c), the contour intervals are 100 years, and the thin lines and shading indicate waters younger than 500 years. In (b) and (d), the contour intervals are 25 years, and the thin lines and shading show negative differences. In (d), in the abyssal ocean the minimum contour level is −50 years, occurring below 4500-m depth at about 65°S.

30–50°N below a depth of 2500 m in ITN2, as indicated by younger waters (up to 350 yr) compared to CONTROL (not shown). This is likely due to a NADW cell that penetrates to slightly deeper depths (Figs. 5d–f) and is accompanied by a 1 Sv increase in MOC in this region. Second, both ITN2 and TN2 show increased ventilation in the Indian Ocean sector of the abyssal Southern Ocean compared to CONTROL. This increase is larger in TN2, as evidenced by up to 50 yr younger waters in Fig. 7d (below 4500-m depth at about 65°S). The local maximum in the Northern Hemisphere in Figs. 7b and d (at about 45°N between 800 and 1000 m depth) is likely due to reduced overturning circulation as shown in Figs. 5d–f. The eddy-induced upwelling rate across 1000-m depth and between 40°S and 45°S is about 2.5 Sv larger in both ITN2 and TN2 than in CONTROL (Figs. 5a–c), thus bringing up older abyssal waters, and contributing to the presence of the Southern Hemisphere local maximum, particularly evident in Figs. 7d at about 45°S above 1000-m depth. At this latitude and depth range, the Eulerian-mean transports do not change appreciably.

The global-mean potential temperature, $\langle\theta\rangle$ in CONTROL (see Table 1) is fortuitously the same as the observational value (Levitus et al., 1998; Steele et al., 2001) computed on our model grid. The $\langle\theta\rangle$ for ITN2 and TN2 are colder than in CONTROL by 0.28 and 0.23 °C, respectively. Most of this cooling, however, occurs in the upper 1000 m, particularly in ITN2, and modestly improves comparisons with observations, as shown by the zonal-mean global potential temperature difference distributions given in Fig. 8. Indeed, we compute 1.82, 1.47, and 1.63 °C as the root-mean-square (rms) model − observations differences for CONTROL, ITN2, and TN2, respectively, in the upper 1000 m. In the tropical regions, the reduction in the warm bias is partly due to a removal of more heat from the near surface ocean as a result of enhanced poleward circulation of the subtropical cells and the associated increase in the return flow bringing colder water into the low latitudes. The increased eddy-induced upwelling rate discussed earlier likely contributes

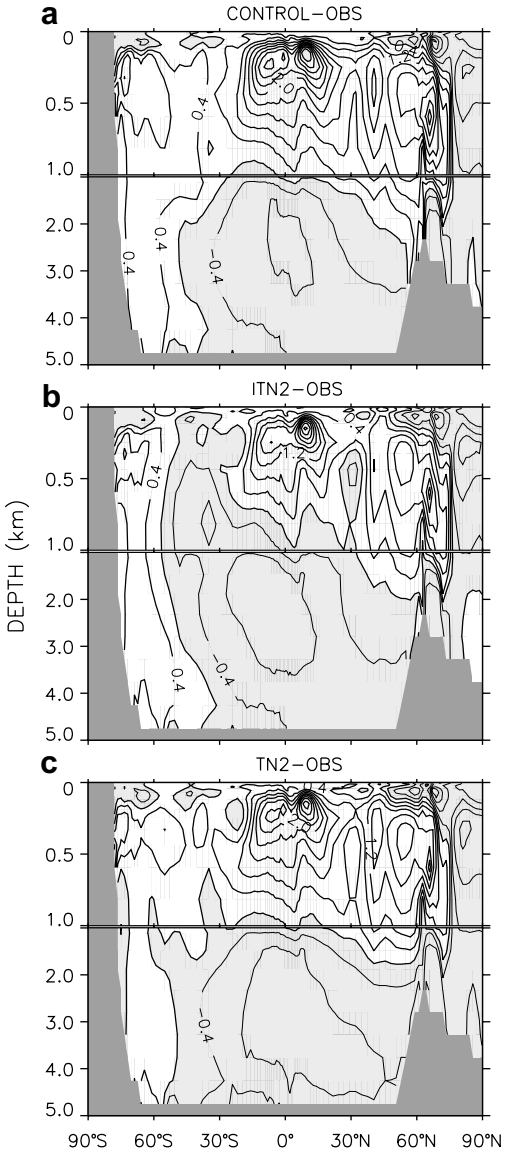

Fig. 8. Time- and zonal-mean, global potential temperature (a) CONTROL − OBS, (b) ITN2 − OBS, and (c) TN2 − OBS difference distributions. The contour interval is 0.4 °C. The thin lines and shading indicate negative differences. OBS represents a blending of Levitus et al. (1998) and Steele et al. (2001) data sets.

to the cooling occurring in the Southern Hemisphere mid-latitudes in both ITN2 and TN2. In all cases, the deep cold bias remains similar, as indicated by the model rms differences from observations (0.73, 0.76, and 0.75 °C for CONTROL, ITN2, and TN2, respectively, below 1000-m depth). We note that all these rms differences represent significant improvements compared to a rms difference of 1.05 °C obtained for a case in which neither the near-surface eddy flux parameterization nor the N^2-dependent diffusivities are used (see Danabasoglu et al. (submitted) for further discussions on abyssal θ changes).

The corresponding zonal-mean potential density differences from observations are presented in Fig. 9. Because the density changes are largely confined to the upper ocean, we use the ocean surface as the reference depth level. Consistent with the upper-ocean cooling, the light bias of CONTROL is significantly reduced in the low- to mid-latitudes of upper 500 m in ITN2. In contrast, TN2 shows similar light biases as in

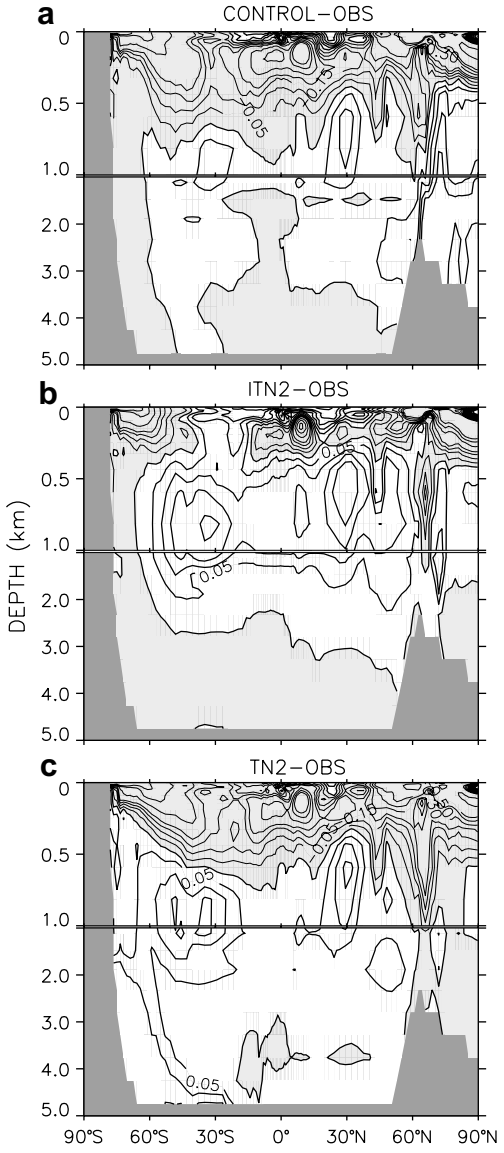

Fig. 9. Time- and zonal-mean, global potential density referenced to surface (a) CONTROL − OBS, (b) ITN2 − OBS, and (c) TN2 − OBS difference distributions. The contour intervals are 0.05, 0.1, and 0.5 kg m^{-3} for differences of less than 0.2, between 0.2 and 0.5, and greater than 0.5 kg m^{-3}, respectively. The thin lines and shading indicate negative differences. OBS is based on a blending of Levitus et al. (1998) and Steele et al. (2001) data sets.

CONTROL here due to compensating effects of reduced θ and reduced salinity. In all cases, the high latitude, upper-ocean density differences mostly reflect salinity changes. In ITN2, the densities are higher than in CONTROL between 500 and 2000 m depth, reflecting cooling in θ. However, below 2000 m, there are no significant density differences, except for some minor changes in its vertical gradients (not shown). The densities in TN2 are generally higher than in both CONTROL and ITN2 in the abyssal ocean, particularly in the Southern Hemisphere high latitudes. Both abyssal cooling (Fig. 8c) and increased salinity contribute to this increase. Unfortunately, the precise source regions for this higher density remain unclear as there are many local changes in the upper-ocean density fields that can have potential effects on abyssal densities. In the zonal-mean comparisons, the upper-ocean densities polewards of 70°S are higher by more than 0.05 kg m^{-3} in TN2 compared to CONTROL.

The model potential temperature distributions along the equatorial Pacific are compared with the Johnson et al. (2002) observational data in Fig. 10. All cases show a largely positive bias with its core rising from a depth of 250 m in the west to about 100 m in the east. This bias is associated with weaker vertical temperature gradients in the model near the core of the Equatorial Undercurrent (EUC). Because these depths are beneath the surface boundary layer, the bias likely indicates that the model background internal wave breaking diffusivity (0.1×10^{-4} m^2 s^{-1}) may be too high. Fig. 10 also shows that there is a modest reduction of this warm bias by 1–1.5 °C in TN2 and ITN2 compared to CONTROL, resulting in a 20–30% reduction in the maximum bias. In TN2 and ITN2, the Eulerian-mean upwelling between 180°E and 260°E in the upper 100 m is larger by about 20–30% than in CONTROL and partially accounts for the reduced warm bias. Compared to the Johnson et al. (2002) data, the EUC structure and speed are well captured in all cases. However, the shallower (by about 20–30 m) EUC core depth in ITN2 compares better with the observations than in CONTROL and

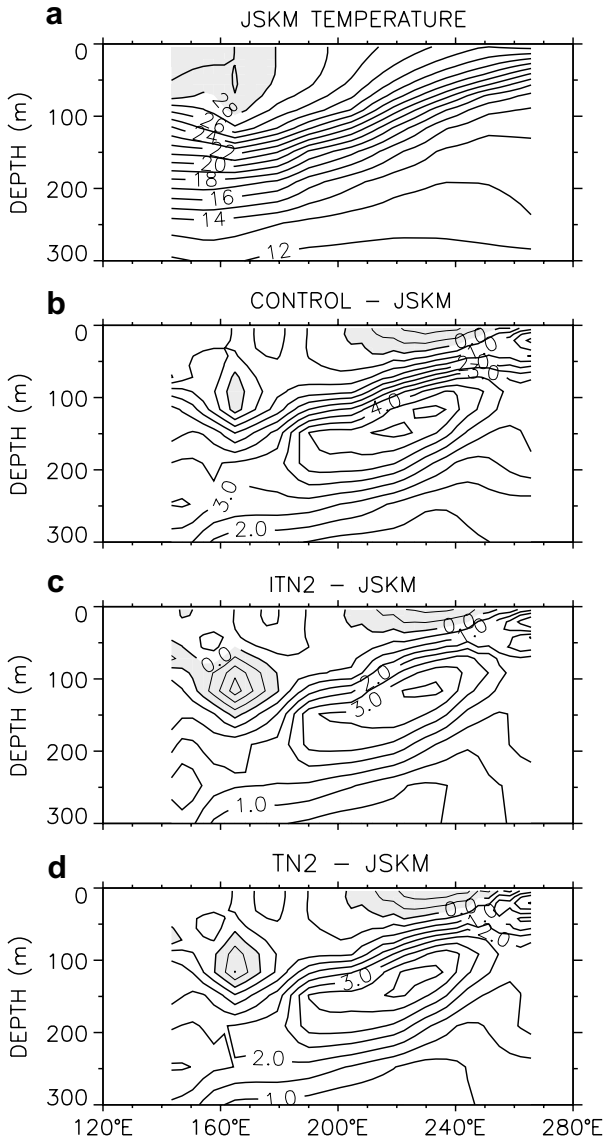

Fig. 10. Time-mean equatorial Pacific potential temperature (a) from Johnson et al. (2002) labeled as JSKM, (b) CONTROL − JSKM difference, (c) ITN2 − JSKM difference, and (d) TN2 − CONTROL difference. The model fields are averaged between 0.6°S and 0.6°N. In (a), the contour interval is 1 °C and regions greater than 28 °C are shaded. In (b–d), the contour interval is 0.5 °C and negative differences (thin lines) are shaded.

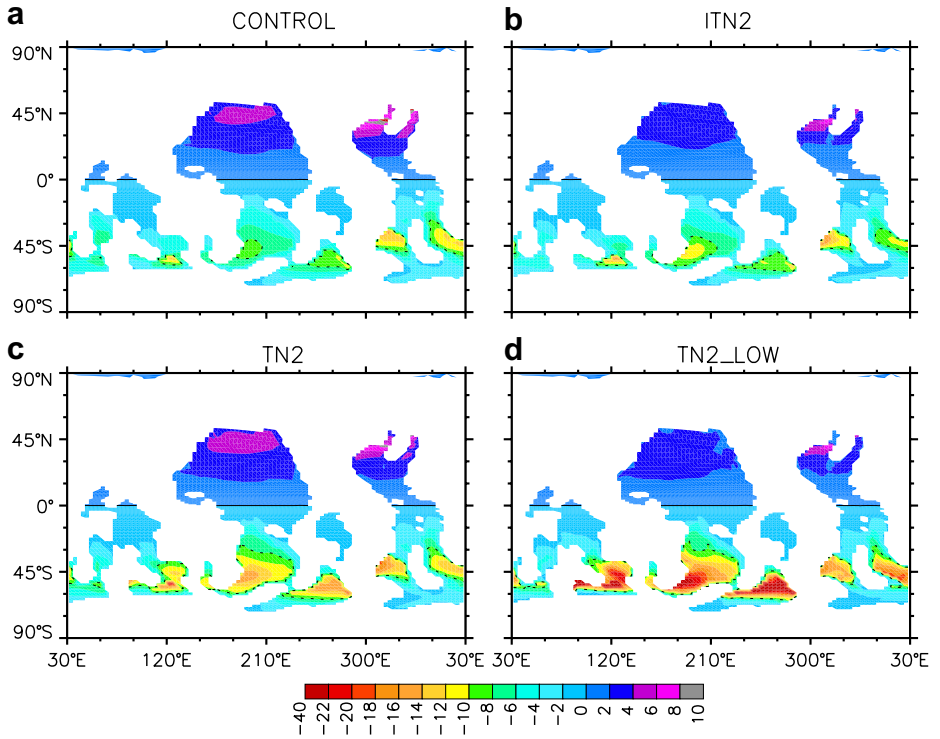

Fig. 11. Time-mean potential vorticity at a depth of 3761 m from (a) CONTROL, (b) ITN2, (c) TN2, and (d) TN2_LOW. The units are 10^{-12} m^{-1} s^{-1} and all panels share the same color scale. The zero and −8 contour lines are indicated by the solid and dotted lines, respectively.

TN2. Otherwise, the maximum zonal velocities are very similar among cases (102, 107, and 101 cm s^{-1} in CONTROL, ITN2, and TN2, respectively).

Finally, we present the potential vorticity, PV, obtained at a depth of 3761 m in Fig. 11 to examine changes in its abyssal distributions. The spatial patterns of PV are similar in all cases with the largest PVs occurring in the Southern Ocean. Because the relative vorticity contribution is rather small in the abyssal ocean, Fig. 11 essentially shows the planetary vorticity, i.e., PV $\approx f/\rho_0(\partial\varrho/\partial z)$, where ρ_0 is a reference density, f is the Coriolis parameter, and ϱ is local potential density. Therefore, the differences between cases simply reflect the changes in $\partial\varrho/\partial z$. For example, in the latitude band of the Southern Ocean, TN2 has a larger $\partial\varrho/\partial z$ (Fig. 9) compared to both CONTROL and ITN2, and hence has a larger PV. These abyssal gradients, i.e., $\partial\varrho/\partial z$, are largest in TN2_LOW (not shown), producing the largest PV magnitudes among the cases (Fig. 11d). In contrast, CONTROL and ITN2 have similar PV magnitudes. Consistent with increased $\partial\varrho/\partial z$ values, there is a monotonic increase in PV magnitudes with lower abyssal A_{ITD} from CONTROL to TN2 to TN2_LOW where A_{I} is kept the same. As evidenced by the ITN2 and TN2 PV distributions, A_{I} can certainly influence PV magnitudes through its direct and indirect effects on model density fields as discussed earlier. The PV magnitudes from TN2 compare rather well with the observational estimates of deep PV provided by O'Dwyer and Williams (1997) based on an earlier version of Levitus et al. (1998) climatology. Rather low A_{ITD} (about 40 m^2 s^{-1}) in the deep ocean in TN2_LOW appears to result in larger PV magnitudes than the estimates. Unfortunately, large observational uncertainties at these high southern latitudes due to poor data coverage precludes a more discriminatory statement about favoring a particular case.

4. Summary and concluding remarks

We have documented the effects of allowing vertical variations of the thickness (and isopycnal) diffusivity coefficients in the climatology of OGCM solutions when compared to observations. Following Ferreira et al.

(2005) we use an N^2-dependent vertical profile that changes in time with the evolving model fields. Such an N^2 dependency provides a convenient way of enhancing diffusivities in the upper ocean and reducing them in the abyss. In our implementation, we employ 4000 $m^2 s^{-1}$ as the reference A_{ITD} within the surface diabatic layer. It is reduced to 400 $m^2 s^{-1}$ by about 2000-m depth. These enhanced surface diffusivities are very much larger than is typically used in models, not inconsistent with recent observations and modeling results (see Marshall et al., 2006; Eden, 2006) and is part of the reason, we believe, for the improvements in our solutions when compared to observed climatologies. The resulting upper-ocean A_{ITD} distributions show that the largest values broadly coincide with the regions of expected intense eddy activity.

Solutions using surface-enhanced diffusivities compare more favorably with the available observations than the solutions from a control case that uses a constant value of 800 $m^2 s^{-1}$ for A_{ITD} and A_I. Indeed, both the vertical structures and the cumulative transports of the eddy-induced velocity in the upper-ocean of the North Pacific obtained using N^2-dependent diffusivities are in remarkably good agreement with the observational estimates of Roemmich and Gilson (2001). Other changes include a reduced warm bias in the upper-ocean, including the equatorial Pacific, and improved southward heat transport in the low- to mid-latitudes of the Southern Hemisphere. These improvements are primarily due to circulation changes. For example, the reduction in the warm bias at low latitudes is due to (i) removal of heat from the near-surface ocean as a result of enhanced poleward transport of the subtropical cells, (ii) the associated increase in the return flow, bringing colder water into the low latitudes, and (iii) increased upwelling at the equator, again bringing colder water from deeper levels in the equatorial Pacific. There is also a modest enhancement of abyssal stratification in the Southern Ocean.

As indicated above, the eddy-induced meridional overturning circulation intensifies near the surface as a result of vertical variations in A_{ITD}. Moreover, the enhanced eddy-induced circulation at the latitude band of the Southern Ocean cancels a greater part of the (Eulerian-mean) Deacon cell. These circulation changes reduce ocean ventilation rates which is likely to have significant consequences for passive tracers.

With the exception of the control case, A_{ITD} varies in the vertical in all our experiments. With regard to A_I, we have considered both spatially uniform and vertically-varying (identical to A_{ITD}) coefficients. Given that there are no strong arguments for setting A_I different from A_{ITD}, we favor making them the same; indeed solutions compare somewhat better with the available observations in our coarse resolution experiments when $A_I = A_{ITD}$.

Our choice of the surface reference value for A_{ITD} is guided by the studies of Ferreira et al. (2005), Ferreira and Marshall (2006), Eden (2006) and Eden et al. (submitted). These also suggest that the diffusivities should be at least an order of magnitude smaller in the deep ocean. In our experience, rather small A_{ITD}, i.e. 40 $m^2 s^{-1}$, in the abyssal ocean leads to oscillations in the model solutions described in the Appendix. Therefore, we recommend that a minimum value is set via Eq. (2). Finally, the horizontal resolution of a model may affect the choice of the A_{ITD} reference values. For example, an argument can be made for lowering A_{ITD} near the equator if a model has adequate resolution to resolve the mesoscale activity there, as recommended by Griffies et al. (2005). In these situations, we recommend using laterally-varying reference diffusivities.

Acknowledgments

We thank Drs. D. Ferreira, P.R. Gent, W.G. Large, and J.C. McWilliams for useful discussions, two anonymous reviewers for helpful comments and suggestions, and Dr. Killworth for his assistance. This research was partially supported by the NSF grant OCE-0336827 for the Climate Process Team on Eddy Mixed-Layer Interactions (CPT-EMILIE). John Marshall acknowledges support from the NASA-funded ECCO2 project and NSF's Polar Program. The computational resources were provided by the Scientific Computing Division of the National Center for Atmospheric Research (NCAR). NCAR is sponsored by the National Science Foundation.

Appendix A. Effects of small diffusivities in the abyssal ocean

When A_{ITD} in the abyssal ocean is as low as 40 $m^2 s^{-1}$, TN2_LOW exhibits a decadal oscillation, particularly prominent in the ACC transport, during the first 250 years of integration. Thereafter, the oscillation

disappears, but the ACC transport monotonically increases, reaching 196 Sv by year 500. A similar oscillatory behavior is also reported in Danabasoglu and McWilliams (1995) when very small values of A_{ITD} are applied in the deep ocean. In general, if A_{ITD} values are reduced, a primary mechanism that flattens isopycnals is diminished. In our experience, this in turn can lead to steeper isopycnals through vertical mixing and eventually to static instability. As a result, both A_{I} and A_{ITD} are further reduced because the numerical diffusive stability criterion (Cox, 1987) forces these coefficients to be severely tapered. The model then resorts to the large convective values of vertical mixing coefficients with no other mixing occurring. Often we observe vertical density profiles close to neutral stability, leading to a persistent near-unstable situation. Introducing additional horizontal diffusivity in these regions does not necessarily alleviate this oscillatory behavior. Based on this previous experience, we believe that the oscillations present in TN2_LOW are due to the positive feedback mechanism described above. We therefore do not recommend using such small A_{ITD} values in the deep ocean.

References

Bauer, S., Swenson, M.S., Griffa, A., Mariano, A.J., Owens, K., 1998. Eddy-mean flow decomposition and eddy-diffusivity estimates in the tropical Pacific Ocean: 1. Methodology. J. Geophys. Res. 103, 30855–30871.

Bryan, K., Lewis, L.J., 1979. A water mass model of the world ocean. J. Geophys. Res. 84, 2503–2517.

Bryan, K., Dukowicz, J.K., Smith, R.D., 1999. On the mixing coefficient in the parameterization of bolus velocity. J. Phys. Oceanogr. 29, 2442–2456.

Bryden, H.L., Imawaki, S., 2001. Ocean heat transport. In: Siedler, G., Church, J., Gould, J. (Eds.), Ocean Circulation and Climate. Academic Press, pp. 455–474.

Canuto, V.M., Dubovikov, M.S., 2006. model of mesoscales in z-coordinates. Ocean Modell. 11, 123–166.

Cox, M.D., 1987. diffusion in a z-coordinate ocean model. Ocean Modelling 74, 1–5 (unpublished manuscript).

Danabasoglu, G., 2004. A comparison of global ocean general circulation model solutions obtained with synchronous and accelerated integration methods. Ocean Modell. 7, 323–341.

Danabasoglu, G., McWilliams, J.C., 1995. Sensitivity of the global ocean circulation to parameterizations of mesoscale tracer transports. J. Climate 8, 2967–2987.

Danabasoglu, G., Large, W.G., Tribbia, J.J., Gent, P.R., Briegleb, B.P., McWilliams, J.C., 2006. Diurnal coupling in the tropical oceans of CCSM3. J. Climate 19, 2347–2365.

Danabasoglu, G., Ferrari, R., McWilliams, J.C., submitted. Sensitivity of an ocean general circulation model to a parameterization of near-surface eddy fluxes. J. Climate.

Dukowicz, J.K., Smith, R.D., 1997. Stochastic theory of compressible turbulent fluid transport. Phys. Fluids 9, 3523–3529.

Eden, C., 2006. Thickness diffusivity in the Southern Ocean. Geophys. Res. Lett. 33, L11606. doi:10.1029/2006GL02615.

Eden, C., Greatbatch, R.J., Willebrand, J., submitted. A diagnosis of thickness fluxes in an eddy-resolving model. J. Phys. Oceanogr.

Ferrari, R., McWilliams, J.C., submitted. Parameterization of eddy fluxes near oceanic boundaries. J. Climate.

Ferreira, D., Marshall, J., 2006. Formulation and implementation of a "residual-mean" ocean circulation model. Ocean Modell. 13, 86–107.

Ferreira, D., Marshall, J., Heimbach, P., 2005. Estimating eddy stresses by fitting dynamics to observations using a residual-mean ocean circulation model and its adjoint. J. Phys. Oceanogr. 35, 1891–1910.

Gent, P.R., 2001. Will the North Atlantic Ocean thermohaline circulation weaken during the 21st century? Geophys. Res. Lett. 28, 1023–1026.

Gent, P.R., McWilliams, J.C., 1990. Isopycnal mixing in ocean circulation models. J. Phys. Oceanogr. 20, 150–155.

Gent, P.R., Willebrand, J., McDougall, T.J., McWilliams, J.C., 1995. Parameterizing eddy-induced tracer transports in ocean circulation models. J. Phys. Oceanogr. 25, 463–474.

Greatbatch, R.J., Lamb, K.G., 1990. On parameterizing vertical mixing of momentum in non-eddy-resolving ocean models. J. Phys. Oceanogr. 20, 1634–1637.

Griffies, S.M. et al., 2005. Formulation of an ocean model for global climate simulations. Ocean Sci. 1, 45–79.

Held, I.M., Larichev, V.D., 1996. A scaling theory for horizontally homogeneous, baroclinically unstable flow on a beta plane. J. Atmos. Sci. 53, 946–952.

Jochum, M., 1997. Eine ortabhaengige Parameterisierung von Wirbelfluessen. Master Thesis. Institut fuer Meereskunde, Kiel.

Johnson, G., Sloyan, B., Kessler, W., McTaggart, K., 2002. Direct measurements of upper ocean currents and water properties across the tropical Pacific during the 1990s. Progr. Oceanogr. 52, 31–61.

Killworth, P.D., 1997. On the parameterization of eddy transfer. Part I. Theory. J. Mar. Res. 55, 1171–1197.

Large, W.G., Yeager, S.G., 2004. Diurnal to decadal global forcing for ocean and sea-ice models. The data sets and flux climatologies. NCAR Tech. Note, NCAR/TN-460+STR, 105 pp. (Available online at http://www.cgd.ucar.edu/oce/pubs/04pubs.html).

Large, W.G., McWilliams, J.C., Doney, S.C., 1994. Oceanic vertical mixing: a review and a model with a nonlocal boundary layer parameterization. Rev. Geophys. 32, 363–403.

Large, W.G., Danabasoglu, G., Doney, S.C., McWilliams, J.C., 1997. Sensitivity to surface forcing and boundary layer mixing in a global ocean model: annual-mean climatology. J. Phys. Oceanogr. 27, 2418–2447.

Large, W.G., Danabasoglu, G., McWilliams, J.C., Gent, P.R., Bryan, F.O., 2001. Equatorial circulation of a global ocean climate model with anisotropic horizontal viscosity. J. Phys. Oceanogr. 31, 518–536.
Ledwell, J.R., Watson, A.J., Law, C.S., 1998. Mixing of a tracer in the pycnocline. J. Geophys. Res. 103, 21499–21529.
Ledwell, J.R., Montgomery, E., Polzin, K., Laurent, L. St., Schmitt, R., Toole, J., 2000. Evidence for enhanced mixing over rough topography in the abyssal ocean. Nature 403, 179–182.
Levitus, S., Boyer, T., Conkright, M., Johnson, D., O'Brien, T., Antonov, J., Stephens, C., Gelfeld, R., 1998. Introduction. Vol. 1, World Ocean Database 1998, NOAA Atlas NESDIS 18, 346 pp.
Marshall, J.C., 1981. On the parameterization of geostrophic eddies in the ocean. J. Phys. Oceanogr. 11, 1257–1271.
Marshall, J.C., 1984. Eddy mean flow interaction in a barotropic ocean model. Quart. J. Roy. Met. Soc. 110, 573–590.
Marshall, J.C., Shutts, G.J., 1981. A note on rotational and divergent eddy fluxes. J. Phys. Oceanogr. 11, 1677–1680.
Marshall, J., Hill, C., Perelman, L., Adcroft, A., 1997a. Hydrostatic, quasi-hydrostatic, and non-hydrostatic ocean modeling. J. Geophys. Res. 102 (C3), 5733–5752.
Marshall, J., Adcroft, A., Hill, C., Perelman, L., Heisey, C., 1997b. A finite-volume, incompressible Navier Stokes model for studies of the ocean on parallel computers. J. Geophys. Res. 102 (C3), 5753–5766.
Marshall, J., Shuckburgh, E., Jones, H., Hill, C., 2006. Estimates and implications of surface eddy diffusivity in the Southern Ocean derived from tracer transport. J. Phys. Oceanogr. 36, 1806–1821.
McWilliams, J.C., Danabasoglu, G., 2002. Eulerian and eddy-induced meridional overturning circulations in the tropics. J. Phys. Oceanogr. 32, 2054–2071.
O'Dwyer, J., Williams, R.G., 1997. The climatological distribution of potential vorticity over the abyssal ocean. J. Phys. Oceanogr. 27, 2488–2506.
Redi, M.H., 1982. Oceanic isopycnal mixing by coordinate rotation. J. Phys. Oceanogr. 12, 1154–1158.
Rix, N.H., Willebrand, J., 1996. Parameterization of mesoscale eddies as inferred from a high-resolution circulation model. J. Phys. Oceanogr. 26, 2281–2285.
Roemmich, D., Gilson, J., 2001. Eddy transport of heat and thermocline waters in the North Pacific: a key to interannual/decadal climate variability. J. Phys. Oceanogr. 31, 675–687.
Smith, R.D., McWilliams, J.C., 2003. Anisotropic horizontal viscosity for ocean models. Ocean Modell. 5, 129–156.
Smith, R.D., Gent, P.R., 2004. Reference manual for the Parallel Ocean Program (POP): ocean component of the Community Climate System Model (CCSM2.0 and 3.0). Tech. Rep. LA-UR-02-2484, Los Alamos National Laboratory, Los Alamos, NM, 75 pp. (Available online at http://www.ccsm.ucar.edu/models/ccsm3.0/pop).
Steele, M., Morley, R., Ermold, W., 2001. PHC: a global ocean hydrography with a high quality Arctic Ocean. J. Climate 14, 2079–2087.
Sundermeyer, M.A., Price, J.F., 1998. Lateral mixing and the North Atlantic Tracer Release Experiment: observations and numerical simulations of Lagrangian particles and a passive tracer. J. Geophys. Res. 103, 21481–21497.
Thiele, G., Sarmiento, J.L., 1990. Tracer dating and ocean ventilation. J. Geophys. Res. 95, 9377–9391.
Treguier, A.M., 1999. Evaluating eddy mixing coefficients from eddy-resolving ocean models: a case study. J. Mar. Res. 57, 89–108.
Treguier, A.M., Held, I.M., Larichev, V.D., 1997. Parameterization of quasigeostrophic eddies in primitive equation ocean models. J. Phys. Oceanogr. 27, 567–580.
Trenberth, K.E., Caron, J.M., 2000. Estimates of meridional atmosphere and ocean heat transports. J. Climate 14, 3433–3443.
Visbeck, M., Marshall, J., Haine, T., Spall, M., 1997. Specification of eddy transfer coefficients in coarse-resolution ocean circulation models. J. Phys. Oceanogr. 27, 381–402.
Whitworth, T., 1983. Monitoring the transport of the Antarctic Circumpolar Current at Drake Passage. J. Phys. Oceanogr. 13, 2045–2057.
Whitworth, T., Peterson, R., 1985. Volume transport of the Antarctic Circumpolar Current from bottom pressure measurements. J. Phys. Oceanogr. 15, 810–816.
Yeager, S.G., Shields, C.A., Large, W.G., Hack, J.J., 2006. The low resolution CCSM3. J. Climate 19, 2545–2566.
Zhurbas, V., Oh, I.S., 2003. Lateral diffusivity and Lagrangian scales in the Pacific Ocean as derived from drifter data. J. Geophys. Res. 108, 3141. doi:10.1029/2002JC00159.